THE DESIGN OF POSTBUCKLING COMPOSITE AEROSPACE STRUCTURES ACCOUNTING FOR DAMAGE INITIATION AND GROWTH

Adrian C. Orifici *,§,[1], Rodney S. Thomson §, Richard Degenhardt ‡, Javid Bayandor **

*** School of Aerospace, Mechanical and Manufacturing Engineering,**
Royal Melbourne Institute of Technology
GPO Box 2476V, Melbourne, Victoria 3001, Australia

§ Cooperative Research Centre for Advanced Composite Structures
506 Lorimer Street, Fishermans Bend, Victoria 3207, Australia

‡ Institute of Composite Structures and Adaptive Systems, German Aerospace Center,
Lilienthalplatz 7, 38108 Braunschweig, Germany

**** Sir Lawrence Wackett Aerospace Centre,**
School of Aerospace, Mechanical and Manufacturing Engineering,
Royal Melbourne Institute of Technology
GPO Box 2476V, Melbourne, Victoria 3001, Australia

Keywords: *Stiffened structures, postbuckling design, interlaminar damage, ply damage*

Abstract

Advanced fibre-reinforced polymer composites have seen a rapid increase in use in aircraft structures in recent years. However, significant conservatism is applied in the design of composite aerospace structures, largely due to the inability of current analysis tools to accurately capture the effect of damage. In this work, the design of fuselage-representative composite structures for postbuckling applications is demonstrated, accounting for damage initiation and growth. An analysis methodology is applied that was developed to capture the critical damage mechanisms leading to collapse of these structures. The analysis methodology is used to investigate the effect of size and location of a pre-existing interlaminar damage region in a postbuckling composite structure design. A pre-damage configuration suitable for experimental investigation is selected. Experimental results are presented of the selected panel configuration tested to collapse in compression, and compared with numerical predictions. The results demonstrate the potential of advanced analysis techniques to reduce the high level of conservatism associated with damage for the design of composite aerospace structures.

1 Introduction

In the design of metallic aircraft structures, the onset of damage is currently allowed within safe operating loads. This is seen in both the acceptance of material plasticity under certain conditions, and the allowance of crack formation and propagation within limits. Allowing the onset of damage in this manner is possible due to a comprehensive understanding of the key damage mechanisms and an ability to accurately predict material behaviour accounting for damage initiation and growth.

Advanced fibre-reinforced polymer composites have seen a rapid increase in use in aircraft structures in recent years due their high specific strength and stiffness, amongst other properties. For the design of composite structures, current analysis tools are unable to give reliable predictions of material behaviour

[1] Corresponding author: a.orifici@crc-acs.com.au

with damage under all conditions. As a result, today's composite structures are designed such that the onset of damage does not occur, and any existing damage must demonstrate "no-growth" behaviour.

In a similar manner, postbuckling design, where lightweight structures are designed to operate safely at loads in excess of buckling, has been applied to metals for decades to design highly efficient structures. However, to date, the application of postbuckling design with composite structures has been limited, as today's analysis tools are not capable of accurately representing the damage mechanisms that lead to structural collapse of composites in compression.

As a result of these considerations, the current design of composite structures is conservative, and a large strength reserve remains unexploited. The currently running four-year European Commission Project COCOMAT [1] is addressing this issue, and aims to allow the onset of damage between limit and ultimate loads in postbuckling composite structures. This is achieved through the development of degradation models capable of accurately representing the critical damage mechanisms contributing to collapse.

In this work, the design of postbuckling composite structures accounting for damage is demonstrated. An analysis methodology is applied that was developed to capture the critical damage mechanisms leading to collapse. This methodology is used in the design of a fuselage-representative postbuckling composite panel containing a pre-existing damage region. The size and location of the pre-damaged region is investigated, and a configuration suitable for experimental testing was selected. Experimental results are presented for a panel containing the selected pre-damage region, and compared to predictions using the analysis methodology. The application of advanced analysis techniques demonstrates the way in which the high level of conservatism associated with damage can be reduced for the design of the next generation of composite aerospace structures.

2 Design Approach

2.1 Design Criterion

For the panels investigated, a research-based focus was applied as the guiding principle behind the design approach. This was based on designing panels suitable for validation of numerical tools. As a result, the design process focused on fuselage-representative panels in which the development of damage was most likely to be stable and measurable in experimental testing.

Based on these considerations, the design focus in this work was to recommend two different damage sizes that were likely to give suitable crack growth properties in experimental testing. In a more industry-based aerospace design environment other criteria such as those based on safe life or damage tolerance considerations would likely be applied [2]. However, the research-based focus applied in this work is suitable to demonstrate the application of damage analysis for the design of postbuckling composite aerospace structures.

2.2 Analysis Methodology

An analysis methodology was applied that was developed to capture the critical damage mechanisms leading to collapse of composite structures [3-4]. The methodology combines separate degradation models for in-plane failure and interlaminar crack growth. This approach has been implemented into the nonlinear finite element (FE) solver MSC.Marc (Marc) with user subroutines, and incorporated into the pre- and post-processing software MSC.Patran (Patran) as a comprehensive analysis tool.

For the ply damage degradation model, an approach based on the Hashin [5] failure criteria and stiffness reduction method of Chang and Lessard [6] was used, as summarised in Table 1, where σ_{11}, σ_{22}, τ_{12} and X, Y, S_{12} are stresses and strengths in the fibre, in-plane transverse and shear directions, S_{23} is the through-thickness shear strength (assumed equal to S_{12} for a transversely isotropic ply), and subscripts T and C refer to tension and compression. The criteria for fibre failure, matrix cracking and fibre-

matrix shear failure were monitored and used to reduce the appropriate material properties to zero upon detection of failure.

In the interlaminar damage growth model, pre-existing interlaminar damage in the skin-stiffener interface was represented as a debonded region between the skin and stiffener. Nominally coincident shell layers were connected with user-defined multi-point constraints (MPCs). The user-defined MPCs were given one of three "states", which were used to define the intact (state 0), crack front (state 1) and debonded (state 2) regions. Gap elements were used in any debonded region to prevent crossover of the two sublaminates.

Table 1. In-plane failure criteria and property reduction

Failure type	Criterion	Property reduced
Fibre, tension	$\left(\sigma_{11}^2/X_T^2\right)^{\frac{1}{2}} \geq 1$	E_{11}, E_{22}, G_{12}, G_{23}, G_{31}
Fibre, comp.	$\left(\sigma_{11}^2/X_C^2\right)^{\frac{1}{2}} \geq 1$	
Matrix, tension	$\left(\sigma_{22}^2/Y_T^2+\tau_{12}^2/S_{12}^2\right)^{\frac{1}{2}} \geq 1$	
Matrix, comp.	$\left(\left(\frac{\sigma_{22}}{Y_C}\left(\frac{Y_C}{4S_{23}^2}-1\right)\right)+\frac{\sigma_{22}^2}{4S_{23}^2}+\frac{\sigma_{12}^2}{4S_{12}^2}\right)^{\frac{1}{2}} \geq 1$	E_{22}
Fibre-matrix shear, tension	$\left(\sigma_{12}^2/S_{12}^2\right)^{\frac{1}{2}} \geq 1$	G_{12}, G_{31}
Fibre-matrix shear, comp.	$\left(\sigma_{11}^2/X_C^2+\sigma_{12}^2/S_{12}^2\right)^{\frac{1}{2}} \geq 1$	

At the end of every nonlinear analysis increment, the Virtual Crack Closure Technique (VCCT) [7] was used to determine the strain energy release rates of all MPCs on the crack front. The onset of propagation was determined using the B-K criterion [8], as given by

$$\frac{G_I+G_{II}+G_{III}}{G_{IC}+\left(G_{IIC}-G_{IC}\right)\left(\frac{G_{II}+G_{III}}{G_I+G_{II}+G_{III}}\right)^{\eta}}=1 \qquad (1)$$

where G are the strain energy release rates in the modes I, II and III, G_C are fracture toughness values, and η is a curve fit parameter found from mixed-mode test data.

For crack propagation, an iterative method was applied. In this method, the VCCT with Equation (1) was used to find any crack front MPCs at which crack growth occurs. The values of G_I, G_{II} and G_{III} were then reduced based on the shape of local crack front to be created. Equation (1) was used again to assess crack growth, and the process repeated until a consistent set of MPCs were found to fail. This iterative method has been found to give more realistic predictions than a simple "fail-release" approach, as it more accurately maintains the VCCT assumption of self-similar crack growth [3-4]

3 Panel Design

3.1 Debond Configurations

The baseline fuselage-representative panel corresponds to COCOMAT Design 1 (D1). This panel is summarised in Fig. 1 and Table 2.

The panel is a multi-stiffener curved design consisting of a skin and blade-shaped stiffeners. In manufacture, half the stiffener lay-up on each side is used to form flanges, which means that the 45 degree flange plies are asymmetric about the stiffener blade. The skin and stiffeners are separately cured then bonded with adhesive.

The panel is loaded statically in compression until collapse. A potting consisting of epoxy resin reinforced with sand and quartz is used at the ends of both panels to ensure an even application of the end loadings and prevent lateral movement in the testing machine.

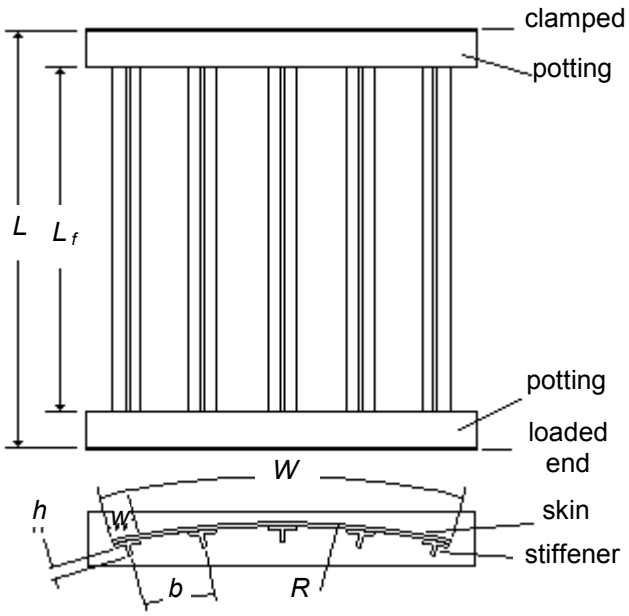

Fig. 1. Panel geometry

Table 2. Panel detail, all dimensions in mm

Number of stiffeners	5
Total length, L	780
Free length, L_f	620
Arc length, W	560
Panel geometry	Curved
Radius, R	1000
Stiffener pitch, b	132
Skin lay-up	$[90,\pm45,0]_S$
Stiffener lay-up	$[(\pm45)_3, 0_6]_S$
Ply material	IM7/8552
Adhesive	FM 300
Ply thickness, t	0.125
Stiffener height, h	14
Stiffener width, w	32

Damage configurations were proposed based on the application of Teflon in the skin-stiffener interface to simulate a debond. The damage configurations were classified according to debond size, location and stiffener, as shown in Fig. 2. Debond size was either 100 mm or 200 mm. For debond location, the panel centreline was designated as location 1 (L1), and there were two other locations (L2 and L3) at 100 mm offset distances from L1. Debonds were located under the centre (C) and an adjacent stiffener (A). As an example, the 100-C-L1 configuration used a 100 mm debond under the centre stiffener at location 1 (the panel centreline).

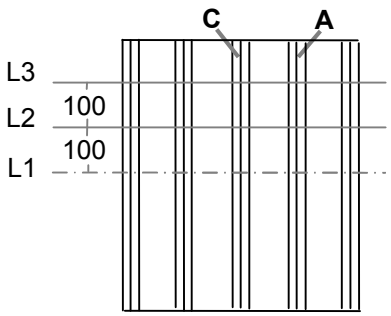

Models
200-C-L1
100-C-L1
100-C-L2
100-C-L3
100-A-L1
100-A-L2
100-A-L3

Fig. 2. Damage configurations, modifying debond size (100,200), location (L1-L3) and stiffener (C,A) (dimensions in mm)

3.2 Analysis

All damage configurations were analysed using only the interlaminar crack growth degradation model described previously. The in-plane ply degradation model was also not applied, as the analysis was focused on comparing the crack growth behaviour of the different configurations.

The FE model for both the centre and adjacent stiffener models consisted of 5772 thick shell elements, 6004 nodes and 395 user-defined MPCs, and is shown in Fig. 3. The skin-stiffener joint of the stiffener containing the debond was modelled using two shell layers, and all other skin-stiffener joints were modelled using a single shell element. This was the only difference between the centre and adjacent stiffener models. The different location models were created by setting the states of the user-defined MPCs accordingly.

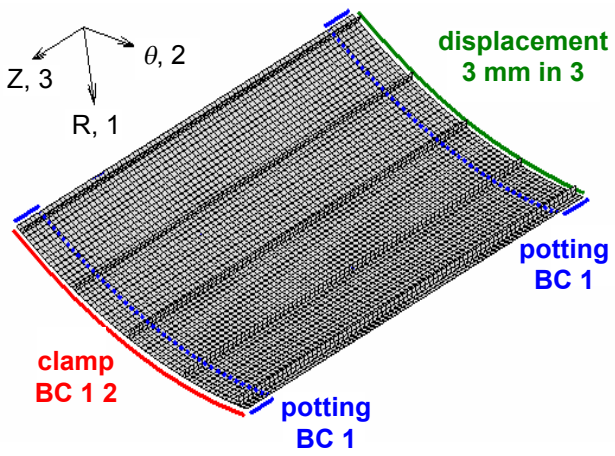

Fig. 3. FE model with boundary condition (BC) definition (MPCs not shown)

The results for the 100 mm and 200 mm L1 proposals are presented below, where Fig. 4 shows both the load and debond length versus applied displacement and the radial displacement at 3.0 mm axial compression. It should be noted that the analyses were only run to 3.0 mm axial compression, as this was not necessary in order to compare the panel configurations from a design perspective and would have increased the computational time considerably. The debond lengths were calculated using the average debond edge locations based on nodal coordinates.

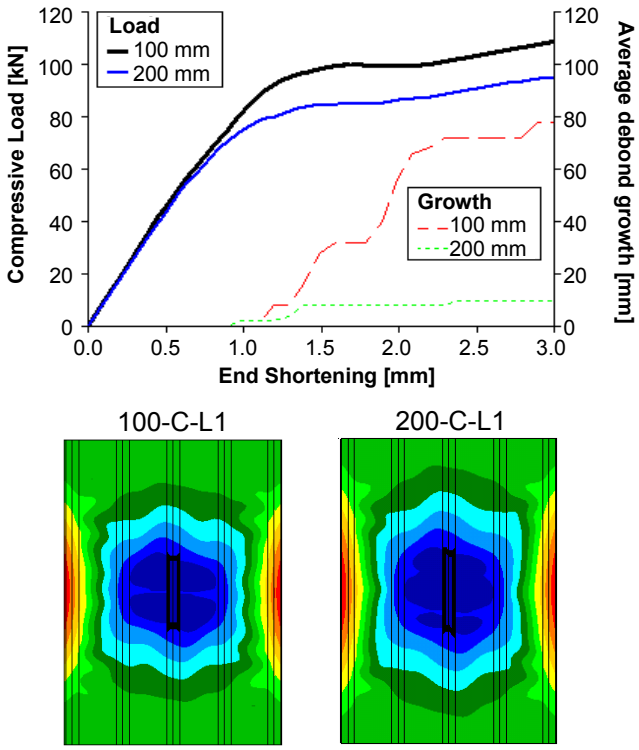

Fig. 4. 100-C-L1 and 200-C-L1 models. Top: Load and debond length versus end shortening. Bottom: Radial displacement and debond at 3.0 mm applied compression

From these results, the 100-C-L1 configuration showed crack growth initiation at 1.2 mm compression coinciding with the onset of global buckling. The global buckling shape consisted of a central buckle over the centre stiffener, with buckling towards the centre of curvature. Crack growth was predicted to occur at both ends of the debonded region throughout the analysis, and was generally symmetric about the panel centreline. The crack growth for this configuration occurred almost exclusively without any mode I component, as crack growth was driven by the shear opening modes II and III. At the end of the 3 mm compression, the size of the debonded area had increased from 100 mm to almost 180 mm.

The 200-C-L1 configuration also showed crack growth initiating around global buckling at 1.1 mm compression, with a single central global buckle over the centre stiffener. Crack growth was again symmetric, and occurred at both ends of the debonded region. However, for this configuration there was much less crack growth predicted throughout the analysis, and at the end of the 3 mm compression the size of the debonded length had only increased from 200 mm to 210 mm.

For the 100 mm debond configurations, offsetting the debond 100 mm to L2 did not affect the global buckling shape, though gave more crack growth than the L1 design that was focused on the debond edge closer to the centreline. Offsetting the debond a further 100 mm to L3 changed the global buckling shape considerably, and also showed a significantly increased crack growth due to the higher proportion of mode I opening displacements at the crack front.

For the debond under the adjacent stiffener, the centreline debond caused a change to an asymmetric global buckling pattern, as the weaker adjacent stiffener buckled inwards first. For all adjacent stiffener models, crack growth initiation was generally coincident with the onset of global buckling, as was seen for the centre stiffener models.

The 100 mm adjacent stiffener debond at L2, shown in Fig. 5, gave a similar asymmetric global buckling shape, though under compression a more symmetric pattern developed with inward global buckles in the outer stiffener bays and an outwards buckling region over the centre stiffener. This displacement shape caused significantly higher mode I component at the crack front of the debond than the L1 design, and as such increased crack growth was seen towards the end of the compression, to give a total crack length of 290 mm.

For the debond at L3, a single central global buckle was again seen, though the diagonal debond placement caused additional mode I opening, and at 3 mm compression the debonded region had extended to cover most of the stiffener length.

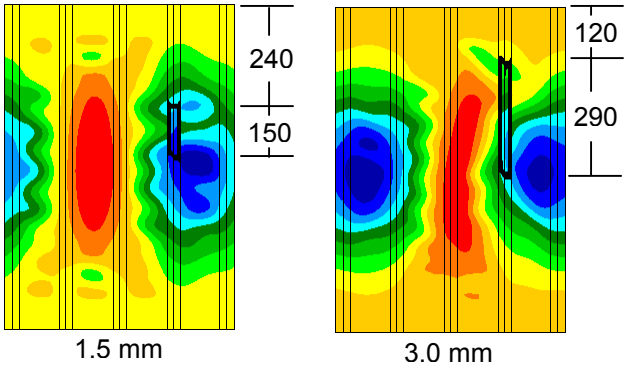

Fig. 5. 100-A-L2 model, out-of-plane displacement and debond size (mm) at applied axial compression

3.3 Design Selection

In terms of using the analysis to make recommendations, the 100 mm L1 configuration with the debond under the centre stiffener showed a significant amount of crack growth occurring in a stable manner throughout the compression, making it suitable for experimental investigation. The 200 mm configuration only showed limited crack growth, and it was concluded that this configuration would offer no new information on crack growth, and was not recommended.

Of the configurations involving the 100 mm debond, the adjacent L2 design was recommended, as it provided stable crack growth, and involved a different global buckling mode shape and a considerably higher mode I component. This allows for the investigation of crack growth at a different mode mixity, and also of the debond behaviour under an asymmetric buckling shape.

4 Experimental Testing

A pre-damaged panel in the 100-C-L1 configuration was manufactured by Aernnova Engineering Solutions and tested by the Institute of Composite Structures and Adaptive Systems of DLR (German Aerospace Center) as part of the COCOMAT project.

The 100 mm debond region was created during manufacture by replacing the adhesive layer with two stips of Teflon. Following manufacture, panel quality was inspected with ultrasonic and thermographic scanning, and no damage was found. Panel imperfection data was measured using the 3D optical measurement system ATOS, with results shown in Fig. 6. During the test, measurements were taken using displacement transducers (LVDTs) and the 3D optical measuring system ARAMIS.

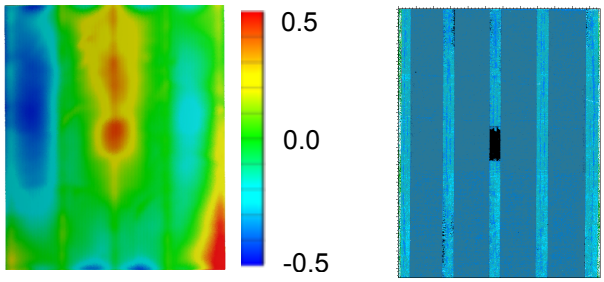

Fig. 6. Experimental panel pre-test inspection data. Left: Radial displacement (mm) from measured radius of 938 mm. Right: Ultrasonic scan

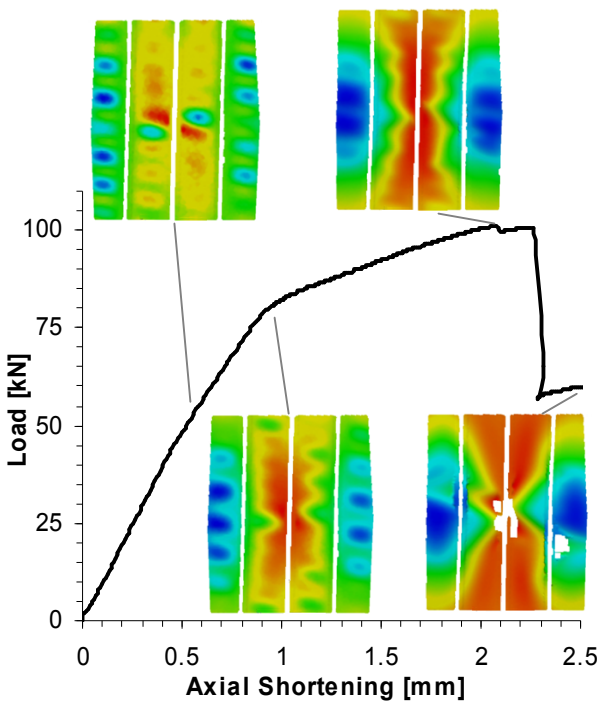

Fig. 7. Experimental load-shortening with radial displacement contours (stiffener side)

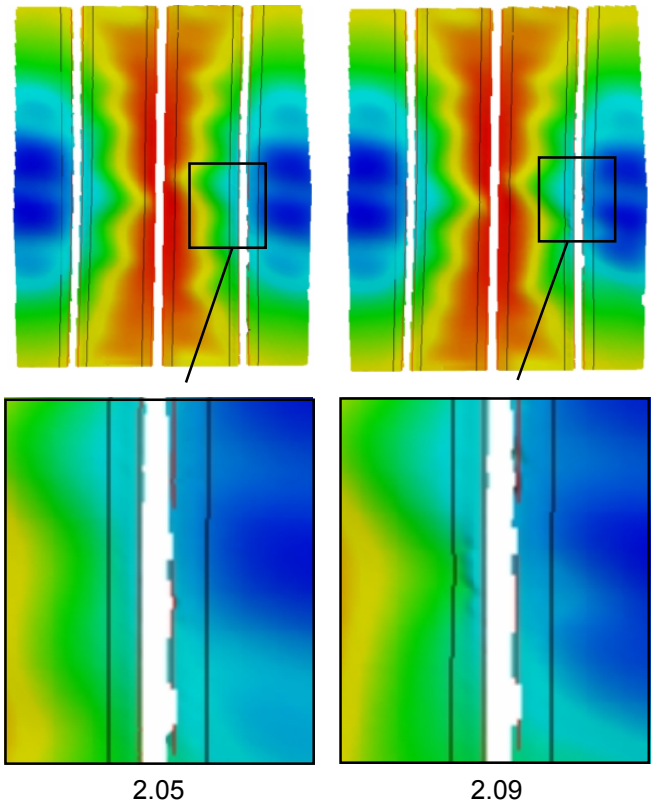

Fig. 8. Experimental panel, radial deformation at applied axial displacement (in mm), showing skin-stiffener debond onset

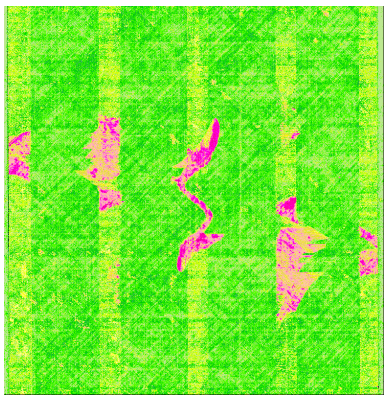

Fig. 9. Experimental panel, post-test ultrasonic scan (stiffener side)

Under compression, the panel developed a range of buckling mode shapes, as shown in Fig. 7. Local buckling (between stiffeners) occurred around 0.50 mm axial compression, with 13 buckling half sine waves in the outer stiffener bays and around 15 half-waves in the inner bays. The pre-damage region led to a diagonal buckling pattern in the panel centre, seen in the upper left image in Fig. 7.

Global (stiffener) buckling was seen at 0.95 mm compression or 80 kN compression load, with the outer stiffener bays buckling towards the stiffeners or panel centre of curvature and the inner bays buckling away from the stiffeners.

At 2.09 mm axial compression a slight drop was seen in the panel load, which appeared to be due to the onset of skin-stiffener debonding at an inner stiffener. This was seen in a local change in buckling pattern, as shown in Fig. 8, and images of the panel showing matrix cracking in the skin in the region.

Final panel collapse was seen at 2.26 mm axial compression or 101 kN compression load, and was caused by skin-stiffener debonding leading to fibre fracture in the stiffeners. The collapsed panel, seen in Fig. 9, showed debond regions under all stiffeners, which were largest for the centre and inner stiffeners.

During testing, cracking was heard just before panel collapse, and this was likely due in part to the skin-stiffener debond onset at 2.09 mm axial compression.

In terms of crack growth, it was difficult to use the 3D optical measurement system to determine crack growth. This was largely due to the order of magnitude difference between the largest out-of-plane displacements and the displacement around the debond region. From all the test data, crack growth from the pre-damage region either did not occur, or occurred just prior to final collapse in combination with skin-stiffener debonding initiating at other locations around the panel.

5 Comparison of Results

The 100-C-L1 numerical model presented previously was analysed using degradation models for interlaminar crack growth and in-plane ply damage. The results are presented below, where Fig. 10 gives the load-displacement curve, Fig. 11 shows the radial displacement and skin-stiffener debond, and Fig. 12 gives the deformed shape and ply failure index at collapse.

In the numerical model, global buckling was predicted at around 1.0 mm axial compression. The predicted buckling mode

shape showed the outer stiffener bays buckling away from the centre of panel curvature, and the centre stiffener buckling towards the centre of curvature. This did not compare well with the experiment, where buckling was seen to occur in the opposite directions.

The FE model also showed postbuckling mode shape changes, where the central global buckle changed location from over the centre stiffener, to inside an inner stiffener bay, and then back over the centre stiffener. These mode shape changes are reflected in the load-displacement curve at 1.6 mm and 2.16 mm axial compression.

In spite of the incorrect buckling mode predictions, the numerical model did give very good comparison with panel stiffness at all stages of loading, and the collapse load of 105 kN compared well with the experimental collapse at 101 kN.

In terms of damage, the numerical predictions were seen to be a function of the postbuckling mode shape, and as such did not compare well with the experiment. Collapse in the FE model was predicted to occur due to fibre fracture in the centre stiffener near the potting and the outer stiffeners near the panel centreline. This occurred at 2.78 mm axial compression, and corresponded to a large reduction in the panel load.

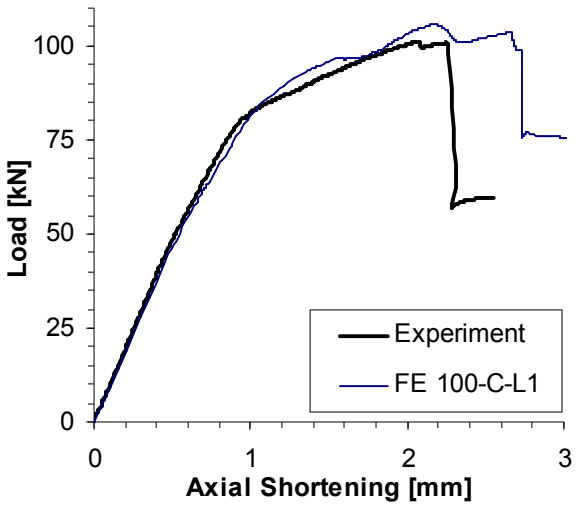

Fig. 10. Load-displacement results, experiment and FE model

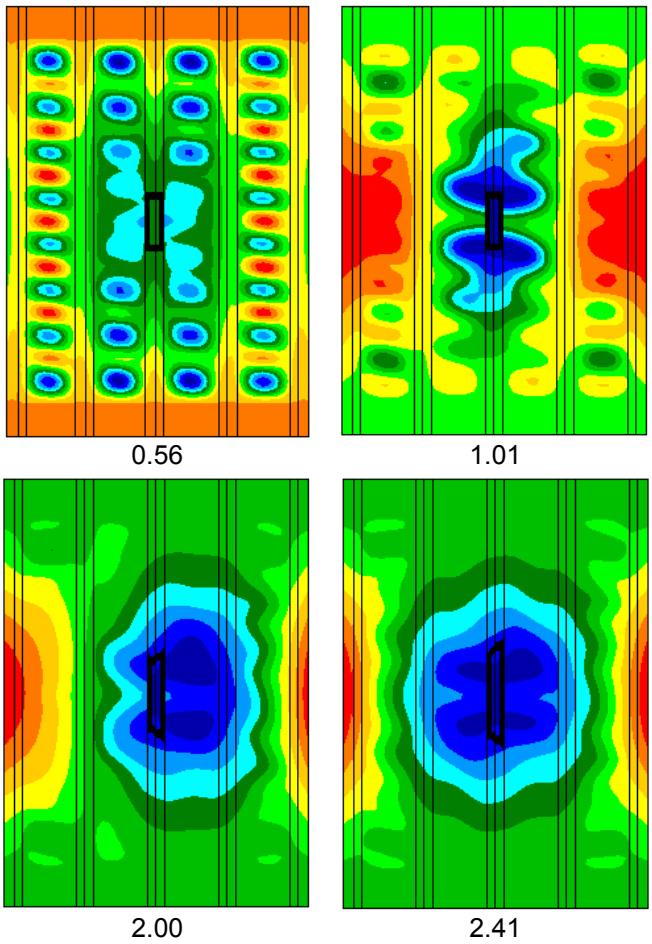

Fig. 11. FE model radial displacements at axial compression (mm), with skin-stiffener debond region shown

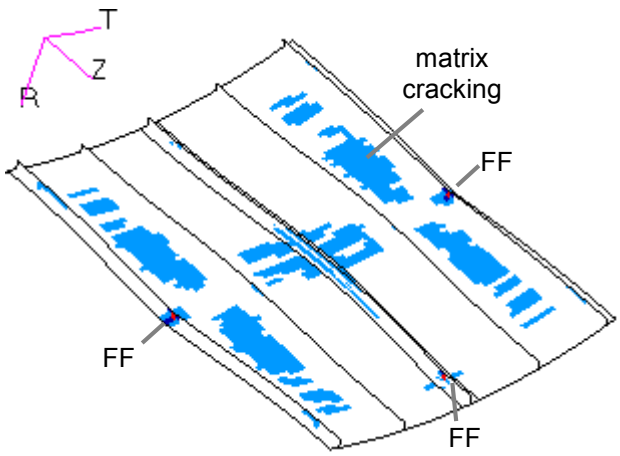

Fig. 12. FE model at collapse (2.78 mm axial compression), deformed shape and ply failure, fibre failure (FF) locations indicated

The numerical model predicted crack growth at the pre-damage region to start at 1.14 mm axial compression, and progress in a stable and continuous manner. At the predicted

collapse at 2.78 mm axial compression pre-damage region had grown from an initial length of 100 mm to around 180 mm. Crack growth was dominated by the shear opening modes II and III, with almost no mode I opening seen, as observed in the previous design analyses.

6 Discussion

The incorrect postbuckling mode shape was the most significant aspect affecting comparison with the experimental results. Though the numerical model still gave good predictions of the panel stiffness and collapse load, the incorrect mode shape significantly influenced the damage predictions.

The most likely reason for the variation in buckling shape between experiment and the FE model is the fact that the numerical model used the nominal geometry and did not account for the real geometric imperfections. The experimental panel radius was found to be 938 mm, which was a significant deviation from the nominal value of 1000 mm. Furthermore, as shown in Fig. 6, the imperfection pattern was asymmetric, appeared influenced by the pre-damage region, and involved out-of-plane displacements of the order of 0.5 mm.

Further analysis on this particular panel would involve taking the geometric imperfection data from the optical measurement system and incorporating this into the FE model. Previous work has illustrated the key nature of panel imperfections on the postbuckling mode shape [9-10]. This includes imperfections in boundary conditions and material properties, and residual stresses. As a result, a more complete design process than presented in this work would consider the panel imperfections, particularly those with the strongest influence on postbuckling shape.

The results in this work indicate that a consideration of variability in real structures should be included as a more integral part of the design process. This would involve analysis of variance techniques such as those presented in Refs [9-10]. The key requirement in this respect would be a robust design that does not show significant change in performance subject to the variation expected in real structures.

The experimental panel demonstrated that the collapse of the pre-damaged panel was due to debond initiation at intact skin-stiffener locations and fibre fracture. Although an analysis methodology encompassing both of these damage mechanisms has been developed [7-8], only interlaminar crack growth was applied in the design process. This was done as the design approach was to compare the pre-damaged configurations in terms of the crack growth behaviour.

The experimental results suggest that even for structures containing a pre-existing skin-stiffener debond, an analysis incorporating all of the damage mechanisms contributing to collapse can be important. However, in this case, as the postbuckling mode shape was so different from the nominal model, considering the additional damage mechanisms would not have provided further information to assist with design.

More generally, this work demonstrated the way in which the design of postbuckling composite aerospace panels can be achieved with a consideration of the key damage mechanisms. This type of design process is dependent on the application of an accurate and validated analysis procedure for the capturing the critical damage mechanisms. Through advanced analysis procedures and an understanding of the way in which the damage mechanisms develop, interact and contribute to collapse, the load-carrying capability of a composite structure can be more reliably predicted. In this way, the high level of conservatism associated with damage can be reduced for the design of the next generation of composite aerospace structures.

7 Conclusion

In this work, the design of postbuckling composite aerospace structures accounting for damage was demonstrated. An analysis methodology for representing interlaminar crack growth and in-plane ply failure was applied.

Various pre-damage configurations were considered by modifying the size and location of a Teflon-generated skin-stiffener debond. The configurations were compared to each design in terms of crack growth behaviour. Two

designs were selected for experimental testing, based on providing suitable crack growth in experiment for validation of numerical tools.

Experimental results were presented for one of the selected pre-damage configurations. Crack growth from the pre-damage was not able to be determined, and the panel failed due to skin-stiffener debonding and fibre fracture.

A comparison of the experimental results with predictions using the analysis methodology was presented. The numerical model was shown to give very good predictions for the panel stiffness and collapse load, despite capturing an incorrect global buckling shape. The incorrect global buckling shape did affect the damage predictions, and the numerical model predicted crack growth from the pre-damage region and collapse due to only fibre fracture.

The results demonstrated the way in which an analysis methodology that captures the critical damage mechanisms can be used as part of a more informative and realistic design process. The accurate prediction of the damage mechanisms leading to collapse of composite structures in compression was discussed as the key to reducing the conservatism associated with damage in composite aerospace structures.

Acknowledgments

The authors would like to acknowledge financial support from the following: the European Commission, Priority Aeronautics and Space, Contract AST3-CT-2003-502723; the Australian Postgraduate Awards Scheme; The CASS Foundation Limited; and, the Australian Government under both the “Innovation Access Programme – International Science and Technology” and “International Science Linkages” established under the innovation statement, “Backing Australia’s Ability”. The work of the staff at the Institute of Composite Structures and Adaptive Systems at DLR Braunschweig is also gratefully acknowledged.

References

[1] Degenhardt R, Rolfes R, Zimmerman R and Rohwer K. COCOMAT – Improved MATerial Exploitation at Safe Design of COmposite Airframe Structures by Accurate Simulation of Collapse. *Composite Structures*, Vol. 73, pp. 178-178, 2006.

[2] Baker A, Dutton, S and Kelly, D. *Composite Materials for Aircraft Structures*. 2nd edition, American Institute of Aeronautics and Astronautics, Virginia, USA, 2004.

[3] Orifici AC, Thomson RS, Degenhardt R and Bayandor J. Development of a finite element methodology for the collapse analysis of composite aerospace structures. *ECCOMAS Thematic Conference on Mechanical Response of Composites*, Porto, Portugal, 12-14 September, 2007.

[4] Orifici AC. *Degradation Models for the Collapse Analysis of Composite Aerospace Structures*. PhD thesis, Royal Melbourne Institute of Technology, 2007.

[5] Hashin Z. Failure criteria for unidirectional composites. *Journal of Applied Mechanics*, Vol. 47, pp. 329-334, 1980.

[6] Chang F-K and Lessard LB. Damage tolerance of laminated composites containing an open hole and subject to compressive loadings: part I − analysis. *Journal of Composite Materials*, Vol. 25, pp. 2-43, 1991.

[7] Rybicki EF and Kanninen MF. A finite element calculation of stress intensity factors by a modified crack closure integral. *Engineering Fracture Mechanics*, Vol. 9, pp. 931-938, 1977.

[8] Benzeggagh ML and Kenane M. Measurement of mixed-mode delamination fracture toughness of unidirectional glass/epoxy composites with mixed-mode bending apparatus. *Composites Science and Technology*, Vol. 56, pp. 439-449, 1996.

[9] Lee M, Kelly D, Orifici AC and Thomson RS. Postbuckling mode shapes of composite stiffened fuselage panels incorporating stochastic variables. *1st CEAS European Air and Space Conference*, Berlin, Germany, 10-13 September, 2007.

[10] Lee MCW, Thomson RS, Degenhardt R and Kelly DW, ‘Imperfection investigation of composite stiffened fuselage panels for postbuckling analyses’, *5th International Conference on Thin-Walled Structures*, Brisbane, Australia, 18-20 June, 2008.

Copyright Statement